ACS APPLIED MATERIALS & INTERFACES

www.acsami.org

Research Article

NiO/Poly(4-alkylthiazole) Hybrid Interface for Promoting Spatial Charge Separation in Photoelectrochemical Water Reduction

Can Lu, Zili Ma, Jakob Jäger, Tetyana M. Budnyak, Richard Dronskowski, Anna Rokicińska, Piotr Kuśtrowski, Frank Pammer, and Adam Slabon*

Cite This: *ACS Appl. Mater. Interfaces* 2020, 12, 29173–29180

Read Online

ACCESS | Metrics & More | Article Recommendations | Supporting Information

ABSTRACT: Conjugated polymers are emerging as alternatives to inorganic semiconductors for the photoelectrochemical water splitting. Herein, semi-transparent poly(4-alkylthiazole) layers with different trialkylsilyloxymethyl (R_3SiOCH_2-) side chains (PTzTNB, R = *n*-butyl; PTzTHX, R = *n*-hexyl) are applied to functionalize NiO thin films to build hybrid photocathodes. The hybrid interface allows for the effective spatial separation of the photoexcited carriers. Specifically, the PTzTHX-deposited composite photocathode increases the photocurrent density 6- and 2-fold at 0 V versus the reversible hydrogen electrode in comparison to the pristine NiO and PTzTHX photocathodes, respectively. This is also reflected in the substantial anodic shift of onset potential under simulated Air Mass 1.5 Global illumination, owing to the prolonged lifetime, augmented density, and alleviated recombination of photogenerated electrons. Additionally, coupling the inorganic and organic components also enhances the photoabsorption and amends the stability of the photocathode-driven system. This work demonstrates the feasibility of poly(4-alkylthiazole)s as an effective alternative to known inorganic semiconductor materials. We highlight the interface alignment for polymer-based photoelectrodes.

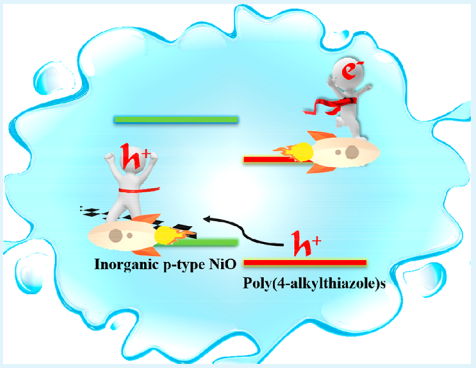

KEYWORDS: *photoelectrochemical water splitting, hydrogen evolution reaction, organic polymers, hybrid materials, photocathodes, inorganic−organic interface*

INTRODUCTION

In view of the often predicted fossil fuel exhaustion and corresponding environment pollution, renewable energy sources have attracted widespread attention.[1−3] In the search for potential candidates, hydrogen produced from solar water splitting is a supposedly clean alternative, owing to its high mass energy density and ease of transportation.[4−7] Photoelectrochemical (PEC) water splitting driven by solar light is an intriguing route to directly convert solar energy into storable hydrogen energy, which is sustainable and potentially economically feasible.[8−10] PEC cells perform redox reactions actuated by charge carriers (electrons and holes) created by incident photons.[11,12] In a photocathode-driven system, disassociated electrons reduce water and evolve hydrogen at the surface of the photocathode and the holes migrate to the counter electrode to oxidize water/hole scavengers, possibly with the assistance of a bias to accelerate the transportation.[13] In light of this, the water reduction efficiency highly depends upon the intrinsic electronic band structure of the photocathode, because it is essentially correlated with the sunlight absorption, charge carrier separation, and photochemical stability.[13]

Although many materials, mainly inorganic semiconductors, have been incorporated in photoelectrodes thus far, the solar conversion efficiency by a bare material remains relatively poor.[14−16] The main drawbacks are the sluggish surface kinetics and insufficient charge carrier utilization as a result of the rapid recombination and slow transfer of photocharges.[17,18] To address these issues, extensive research strategies, especially for heterojunction engineering, have been exploited to alleviate these obstacles.[19−22] A Si photocathode functionalized by a GaN layer presented, for instance, 10.5% applied bias photon-to-current efficiency and a large current density surpassing 35 mA cm^{-2} at 0 V_{RHE} under 1 sun illumination, profiting from the significantly reduced charge transfer resistance at the semiconductor/liquid junction.[8] Nevertheless, the finite integration structure confined by the numerable inorganic semiconductors prohibits the future widespread development of hydrogen generation.[23] From all of the solutions that have been accepted to improve the performance of photocathodes to date, adopting organic polymers with semiconductor

Received: March 1, 2020
Accepted: June 3, 2020
Published: June 3, 2020

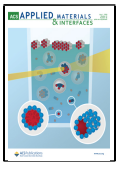

https://dx.doi.org/10.1021/acsami.0c03975
ACS Appl. Mater. Interfaces 2020, 12, 29173−29180

properties to build composite photoelectrodes has only yet rarely been addressed.[24]

Conjugated polymers are promising to revise the behavior of conventional photoelectrodes as a result of the probability of tailoring the optical, electric, and morphological features at the molecular level.[3,24] Miyauchi et al. coated with poly(3,4-ethylenedioxythiophene) (PEDOT) a CdS and CdSe quantum-dot-sensitized TiO_2 photoelectrode, which helped to prevent the photocorrosion and to mitigate the recombination, leading to an upgraded photocurrent of approximately 15 mA cm^{-2} in the absence of applied bias.[25] On the other hand, a recent work by Xu et al. used polythiophene to passivate the surface states of the $CuBi_2O_4$ photocathode. The composite electrode yielded a 2-fold higher photocurrent as a result of enhanced light-trapping ability and facilitated charge carrier separation.[26]

In this work, we have built hybrid photocathodes by integrating a conjugated polymer layer (Scheme 1) with p-type

Scheme 1. Synthesis of PTzTNB and PTzTHX

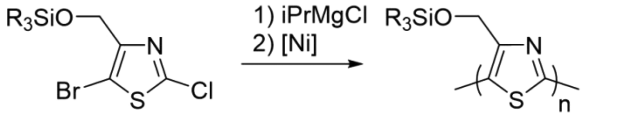

1a, R = *n*-Butyl
1b, R = *n*-Hexyl
PTzTNB, R = *n*-Butyl
PTzTHX, R = *n*-Hexyl

NiO thin films. The poly(4-alkylthiazole)s, which we have synthesized previously,[27,28] are characterized by a backbone chain with alternating single and double bonds. The overlapping π orbitals create a conjugated system containing delocalized π electrons, which is responsible for their distinct photochemical and electronic properties.[23,24] The heterojunction interface contributes to the photoexcited electron–hole pair separation. The synergistic effect based on inorganic NiO and conjugated poly(4-alkylthiazole)s enhances water reduction activity.

EXPERIMENTAL SECTION

Synthesis of NiO Thin-Film Electrodes. NiO thin films were hydrothermally grown on fluorine-doped tin oxide (FTO)-coated glasses (2.2 mm thick, Sigma-Aldrich). The FTO substrates were ultrasonically cleaned in acetone, ethanol, and deionized (DI) water for 10 min each prior to use. For a typical hydrothermal process, 0.4 g of nickel acetate tetrahydrate and 0.22 g of hexamethylenetetramine were dissolved in 28 mL of DI water under vigorous stirring for 30 min to form a laurel green transparent solution. The resulting solution was then averagely divided and transferred to four 20 mL Teflon-lined autoclaves, where FTO substrates were aslant-placed against the wall, with the conducting side facing down. The hydrothermal reaction was conducted at 383 K for 6 h with a ramping rate of 2 K min^{-1}. The resultant substrates with a thin layer coating were subsequently washed and finally thermally treated at 723 K for 30 min to obtain NiO electrodes.

Fabrication of NiO/Poly(4-alkylthiazole) (PTzTNB and PTzTHX) Composite Photocathodes. The polymers PTzTNB and PTzTHX were synthesized according to a previously reported route (Scheme 1).[27] Starting from 2,5-dihalogenated thiazoles (1a/1b), the polymers were obtained by nickel-catalyzed Kumada-coupling polycondensation of *in situ* generated bifunctional monomers. For the tetrahydrofuran (THF)-soluble fraction of PTzTNB, a number-average molecular weight (M_n) of 10.7 kg mol^{-1} and a polydispersity (PDI) of 2.22 were determined by gel permeation chromatography in THF. Because PTzTNB is not fully soluble in THF, the molecular weight of the bulk material is presumed to be higher. PTzTNB is fully soluble in $CHCl_3$, which was used for spin coating. A fully soluble batch of PTzTHX with M_n = 29.6 kg mol^{-1} and a PDI of 2.4 was used. A thin and compact PTzTNB or PTzTHX layer was then spin-coated on as-obtained NiO electrodes at 600 rmp using corresponding poly(4-alkylthiazole) solution (5 mg mL^{-1} in chloroform). The electrodes were finally dried at room temperature and kept for further use. PTzTNB and PTzTHX were also spin-coated identically on bare FTO substrates as contrasts.

Characterization. Powder X-ray diffraction (PXRD) experiments were performed in transmission mode using a calibrated STOE STADI-P powder diffractometer with Cu Kα_1 radiation. The surface and cross-section morphology of the photocathodes was characterized by scanning electron microscopy (SEM, Leo Supra 35VP SMT, Zeiss). A spectrophotometer (Shimadzu, UV-2600) was employed to evaluate the optical property of as-obtained thin films. X-ray photoelectron spectrometry (XPS, Prevac) equipped with a hemispherical analyzer (VG SCIENTA R3000) was used to verify the surface composition. The spectra were recorded with a monochromatized aluminum source Al Kα (E = 1486.6 eV) and calibrated using the Au $4f_{7/2}$ line of a cleaned gold sample at 84.0 eV.

PEC Measurements. The PEC performances of all photocathodes were evaluated in a typical three-electrode configuration: the fabricated photoelectrode as the working electrode, a platinum wire electrode as the counter electrode, and a 1 M Ag/AgCl electrode as the reference electrode. The PEC measurements were conducted under back-side Air Mass 1.5 Global (AM 1.5G) illumination (100 mW cm^{-2}, class-AAA 94023A, Newport), and 0.1 M phosphate buffer (KP_i, pH 7) mixed with acetonitrile ($V_{KPi}/V_{acetonitrile}$ = 9:1) degassed by N_2 was used as electrolyte throughout the work. $K_2S_2O_8$ (0.1 M) was used as the electron scavenger in the electrolyte for experiments related to determination of the charge carrier separation.[29]

Linear sweep voltammetry (LSV) at a scan rate of 10 mV s^{-1} and chronoamperometry (CA) at 0 V_{RHE} were measured by a potentiostat (PalmSens4, PalmSens BV), and the potentials were finally adjusted to E_{RHE} based on the Nernstian relation ($E_{RHE} = E^0_{Ag/AgCl} + 0.059\ V \times pH + E_{Ag/AgCl}$). The Mott–Schottky and electrochemical impedance spectroscopy (EIS) characterizations were carried out by a Gamry Interface 1010T potentiostat/galvanostat/ZRA workstation. Specifically, a 10 mV amplitude was applied on the Mott–Schottky test at frequency of 100 Hz in dark conditions. The EIS was documented at a direct current (DC) bias of 0.1 V_{RHE} in the frequency range from 20 kHz to 0.2 Hz.

RESULTS AND DISCUSSION

Structure and Morphology. Hydrothermally synthesized NiO is phase pure and crystallizes with a cubic phase [Joint Committee on Powder Diffraction Standard (JCPDS) 73-1519], as observed from the PXRD patterns (Figure S1a of the Supporting Information). The SEM image reveals a thin sheet-like structure of the pristine NiO thin film (Figure S1b of the Supporting Information). The high-density NiO nanosheets with an average thickness of tens of nanometers are perpendicularly oriented to the substrate in a homogeneously and decussately sheet-piled distribution. Figure S1c of the Supporting Information exhibits the digital photo of the as-synthesized NiO photocathode.

Panels a–d of Figure 1 correlate the top-view SEM images of the NiO/PTzTNB photocathode under different magnifications. Thin and semi-transparent PTzTNB layers homogeneously lie on the top of the nanosheets while still retaining partial exposure of inner hierarchical NiO as a result of the low loading content. Such a configuration is suited for the sufficient utilization of solar light of both photoactive components.[30] The layered characteristic of the deposited poly(4-alkylthiazole)s can also be seen in our previous work.[27] The cross-sectional images in close shot (Figure 1e) and distant

https://dx.doi.org/10.1021/acsami.0c03975
ACS Appl. Mater. Interfaces 2020, 12, 29173–29180

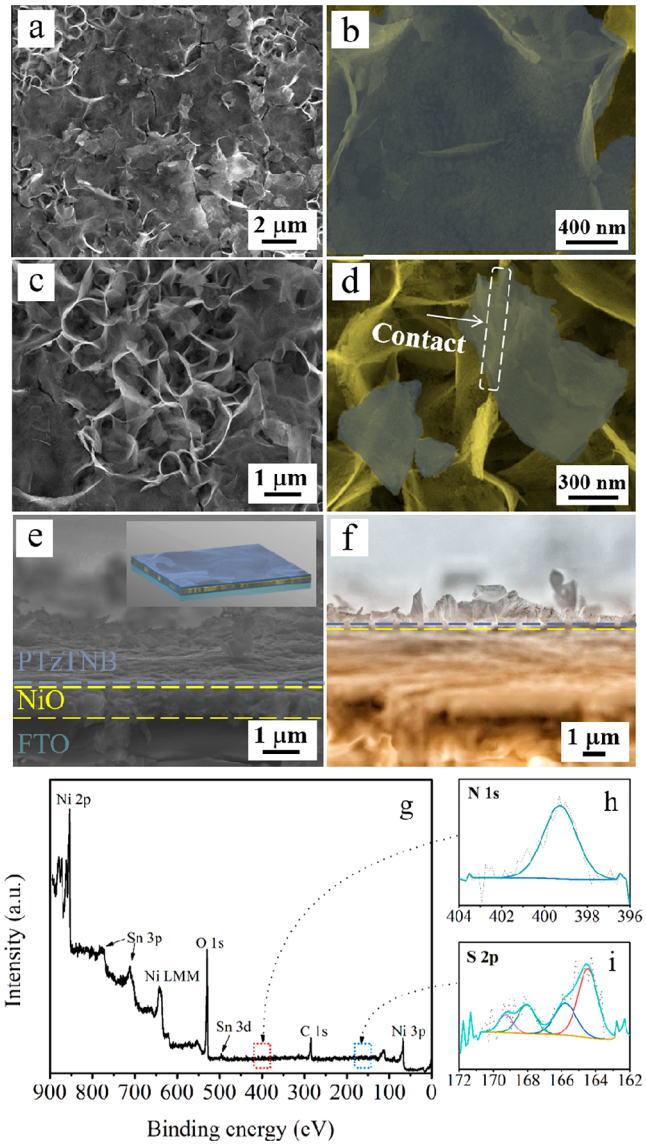

Figure 1. (a–d) Top-view SEM images of the NiO/PTzTNB photocathode. The yellow and violet areas in panels b and d represent the existence of NiO and PTzTNB, respectively. (e and f) Side-view SEM images (inset: sketch map of the NiO/PTzTNB photocathode). (g) Survey XPS spectrum, (h) core level N 1s, and (i) S 2p XPS spectra of the NiO/PTzTNB photocathode.

view (Figure 1f) further manifest the layered structure of the hybrid, where the NiO film with an average thickness of ca. 1 μm was grown on the FTO substrate and covered by a thin PTzTNB overlayer with the mean thickness of several tens of nanometers.

To further identify the surface composition upon coating, XPS was employed to characterize the chemical state of the NiO/PTzTNB photocathode. In the survey spectrum (Figure 1g), all expected lines attributed to the main components of the studied material are detected. The C 1s, N 1s (Figure 1h), and S 2p (Figure 1i) peaks clearly confirm the presence of PTzTNB deposited on the FTO/NiO support. In the C 1s region, the dominant peak, typical of sp^3 carbon atoms from the side alkyl chains, is located at 284.5 eV, but the shoulder at higher binding energies confirms the presence of C atoms attached to heteroatoms (especially highly electronegative N and O). Furthermore, the N 1s peak at 399.3 eV corresponds to the thiazole nitrogen atoms,[31] whereas the S $2p_{3/2}$ and S $2p_{1/2}$ peaks at 164.5 and 165.8 eV, respectively, fit well to sulfur in thiophene-like species.[32] The appearance of one additional S 2p doublet at 168.0 and 169.3 eV may, in turn, suggest a partial conversion of S to oxidized species. It should be emphasized that both the C/S (13.9) and C/N (21.4) atomic ratios are roughly close to those expected for the ideal 4-alkylthiazole molecules. Additionally, the C/Ni, N/Ni, and S/Ni atomic ratios of the hybrid photocathode are determined to be 0.56, 0.03, and 0.06, respectively.

Optical Property and Electronic Band Structure. The UV–vis transmittances of FTO/PTzTNB and FTO/PTzTHX are greater than approximately 60% in the range between 360 and 800 nm, except for the characteristic absorption from poly(4-alkylthiazole)s (Figure 2a). Coupling the latter to NiO

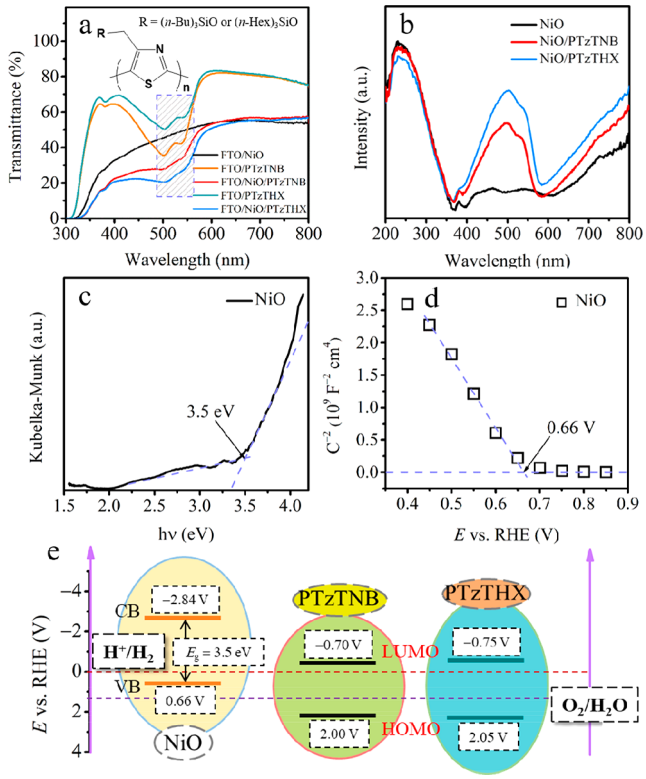

Figure 2. (a) Optical transmittance spectra and (b) absorption spectra of the samples. (c) Kubelka–Munk-transformed reflectance spectrum of NiO. (d) Mott–Schottky plot of NiO recorded at 100 Hz in the dark. (e) Sketch maps of the electronic band structures of NiO, PTzTNB, and PTzTHX.

broadens the light absorption range and enhances the light-harvesting efficiency (Figure 2b), which especially manifests in the emergence of the intrinsic photoabsorption of poly(4-alkylthiazole)s from 400 to 600 nm. After integration of poly(4-alkylthiazole)s with NiO, the photocathodes still maintain relatively high transmittance.

The band gap of NiO is determined to be 3.5 eV according to the Kubelka–Munk-transformed reflectance spectrum (Figure 2c). The negative slope of the Mott–Schottky plot indicates the p-type nature of the NiO film (Figure 2d). Generally, the potential of the valence band edge (E_{VB}) for a p-type semiconductor is considered to be approximate to the flat band potential (E_{fb});[33] the E_{VB} is thus estimated to be 0.66 V_{RHE} (Figure 2d). The potential of the conduction band edge

https://dx.doi.org/10.1021/acsami.0c03975
ACS Appl. Mater. Interfaces 2020, 12, 29173–29180

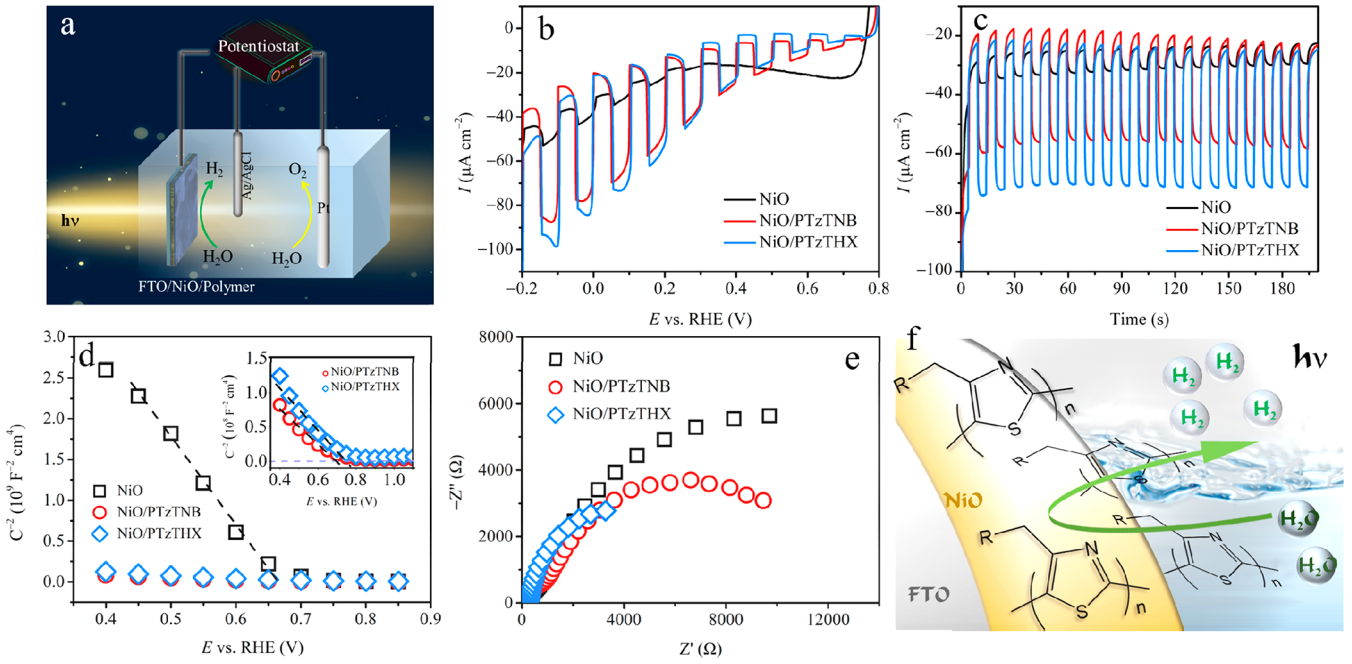

Figure 3. (a) Schematic of the hybrid water-splitting electrochemical cell. (b) LSV and (c) CA curves of NiO, NiO/PTzTNB, and NiO/PTzTHX photocathodes under interrupted AM 1.5G illumination. (d) Mott−Schottky plots of NiO, NiO/PTzTNB, and NiO/PTzTHX photocathodes recorded at 100 Hz in the dark (inset: enlarged Mott−Schottky plots of NiO/PTzTNB and NiO/PTzTHX photocathodes). (e) EIS Nyquist plots of NiO, NiO/PTzTNB, and NiO/PTzTHX photocathodes acquired at 0.1 V_{RHE} and frequency from 20 kHz to 0.2 Hz. (f) Schematic diagram of the NiO/poly(4-alkylthiazole)s photocathodes and surface hydrogen-evolving process.

(E_{CB}) is then calculated to be −2.84 V_{RHE} by combining with the determined band gap value (Figure 2e). Additionally, the highest occupied molecular orbital (HOMO) levels and lowest unoccupied molecular orbital (LUMO) levels on the Fermi energy scale were determined to be −6.06 and −3.35 V for PTzTNB and −6.11 and −3.30 V for PTzTHX, respectively.[27] The HOMO and LUMO potentials are finally converted to the values in the RHE scale,[34] which are depicted in Figure 2e. The hybrid architectures present a favorable energetic alignment, matching the potential needed for efficient proton reduction. The staggered energy levels between NiO and poly(4-alkylthiazole)s afford a potential gradient to spatially disassociate the photogenerated charge carriers and suppress their recombination (*vide infra*).[35−37]

Photoelectrochemistry. The PEC water reduction performance was assessed over the NiO/poly(4-alkylthiazole)s thin-film photocathodes in a three-electrode configuration under back-side AM 1.5G illumination (Figure 3a). Panels b and c of Figure 3 exhibit the interrupted LSV and CA curves at 0 V_{RHE}, respectively. As a result of the hydrophobicity of the poly(4-alkylthiazole)s, acetonitrile in 10% volume ratio was added to the 0.1 M KP_i aqueous electrolyte to ameliorate the wettability of the photocathode surface. The pristine NiO photocathode generates a typical cathodic photocurrent with an onset potential of ca. 0.4 V_{RHE} in Figure 3b. The net photocurrent density at 0 V_{RHE} is approximately 9 μA cm^{-2}, suggesting the low efficiency to stem from the sluggish photogenerated electron−hole pair disassociation.[38,39] The dark current (ca. 31 μA cm^{-2}) has also been reported in related work based on NiO[40,41] and can be attributed to possible partial reduction of the metal oxide[40,42] or contribution toward electrocatalytic reduction of water. Panels a and b of Figure S2 of the Supporting Information compare the transient photocurrents of the pristine poly(4-alkylthiazole)s photocathodes by means of intermittent-illuminated LSV and CA curves, respectively. PTzTNB and PTzTHX exhibit onset potentials at ca. 0.4 and 0.5 V_{RHE}, and net photocurrent density of 8 and 20 μA cm^{-2} at 0 V_{RHE}, respectively. The higher photocurrent and earlier onset hint toward the better proton reduction efficiency of PTzTHX in comparison to PTzTNB. The better PEC behavior of the former can be attributed to the lower transfer resistance (*vide infra*).[27] It is worth noting that the two poly(4-alkylthiazole)s were deposited on FTO with the same procedure as the inorganic−polymer composite electrodes. The noticeable dark current of the two pristine photocathodes (Figure S2a of the Supporting Information) is therefore mainly ascribed to the relative low coating amount that is inadequate to fully block the underlying FTO substrates (Figure S3 of the Supporting Information). In addition, a complementary 8 h CA measurement (Figure S4 of the Supporting Information) was also implemented to evaluate the long-term stability of bare PTzTHX on bare FTO without the NiO layer and further identify the underlying origin of the dark current. The photocurrent density decay is connected to the low mechanical stability on the bare FTO surface, if no NiO layer is present, and additional charge accumulation in the PTzTHX layer.[43,44]

Substantial improvements on the photocurrent and onset potential are achieved upon spin-coating poly(4-alkylthiazole)s thin layers, as shown in panels b and c of Figure 3. The NiO/PTzTNB and NiO/PTzTHX photocathodes reveal 50 and 60 μA cm^{-2} net photocurrent densities at 0 V_{RHE}, respectively, corresponding remarkably to a 4.6 and 5.7 times enhancement if compared to the pristine NiO photocathode (Figure 3b). This implies that pairing PTzTHX with NiO contributes more to the photocurrent augment relevant to PTzTNB. In addition, upon loading poly(4-alkylthiazole)s, the onset of the photocurrent also shifts positively to approximately 0.8 V_{RHE} (Figure 3b and Figure S5 of the Supporting Information). The

https://dx.doi.org/10.1021/acsami.0c03975
ACS Appl. Mater. Interfaces 2020, 12, 29173−29180

persistence of the dark current in Figure 3b is correlated with the incomplete blocking of inner NiO as a result of the limited polymer-loading content (Figure 1).[45] A similar dark current has also been reported in polymer-based photocathode-driven systems.[26,43,44] Additionally, amended stability is realized after functionalization with PTzTHX, which manifests in the almost unaltered photocurrent during CA (Figure 3c).

Mechanistic Investigations. To identify the inner kinetics on the augmented hydrogen generation, Mott–Schottky analysis derived from the electrochemical impedance were performed at 100 Hz in the dark (Figure 3d). The diminished slopes for NiO coupled with poly(4-alkylthiazole)s indicate the enhancement of the charge carrier density.[46] Furthermore, the positive shift of E_{fb} (Figure 3d) was reported to be associated with the enlarged band bending at the electrode/electrolyte interface based on the equation[17,47]

$$E_b = E - E_{fb} \quad (1)$$

where E_b correlates the magnitude of the band bending and E is the applied bias potential, which is normally negative for proton reduction. Because the higher band bending at the interface is indicative of accelerated carrier separation and a prolonged electron lifetime,[12,48,49] the electron–hole recombination is thus mitigated through poly(4-alkylthiazole)s coupling.

Electronic transport kinetic analysis based on EIS Nyquist plots further verifies the improved photogenerated electron–hole pair disassociation and migration (Figure 3e). The apparently reduced radius of the semicircular arc on the hybrid photocathodes reveals the much smaller resistance for charge transfer, relative to the bare NiO photocathode.[50−52] The complementary EIS Nyquist plots for PTzTNB and PTzTHX are presented in Figure S6 of the Supporting Information. The higher photocurrent (Figure S2 of the Supporting Information) for bare polythiazole electrodes, which were equipped with $(n\text{-Hex})_3SiOCH_2-$ in comparison to $(n\text{-Bu})_3SiOCH_2-$, is reflected in the smaller charge transport resistance for PTzTHX.

To further quantify the contribution of poly(4-alkylthiazole)s to the alleviated carrier recombination, a complementary experiment was also performed to evaluate the efficiency of charge carrier separation ($\eta_{separation}$) in the bulk and surface charge transfer ($\eta_{transfer}$) with respect to the photocathodes NiO and NiO/PTzTNB. The obtained net photocurrent curves recorded in the electrolyte without and with $K_2S_2O_8$ as the electron scavenger are shown in Figure S7 of the Supporting Information, which were then employed to calculate $\eta_{separation}$ and $\eta_{transfer}$, assuming the electronic bandgap of NiO as the reference value (Figure S8 of the Supporting Information).[53] Apparently, depositing PTzTNB on the NiO electrode leads to an enhancement of $\eta_{separation}$, especially in the potential range between −0.1 and 0.4 V_{RHE}, benefiting from the formation of heterojunction interfaces (*vide infra*). Additionally, a percentual increase of $\eta_{transfer}$ can be observed for the heterojunction photocathode. These enhancements eventually lead to an augmented PEC water reduction. Therefore, the interfacial effects within the heterojunctions are integrally responsible for the remarkably enhanced charge carrier separation and mobility as well as the raised electron density and prolonged lifetime. Figure 3f depicts the schematic of the NiO/poly(4-alkylthiazole) photocathodes and illustrates the surface hydrogen evolution reaction.

On the basis of the determined band edge positions and the p-type nature of both the inorganic and organic components, the Fermi level (E_F) of NiO is estimated to be higher than that of poly(4-alkylthiazole)s. Figure 4a schematically illustrates the

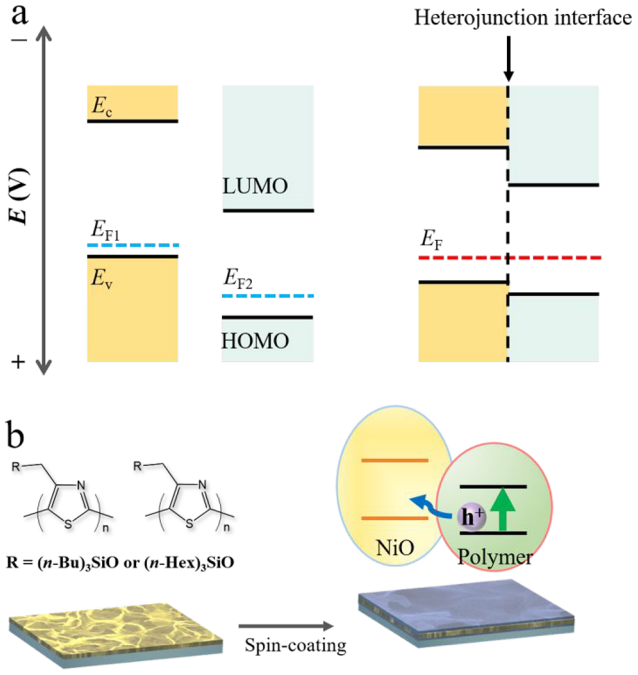

Figure 4. (a) Schematic energy band diagrams of NiO, poly(4-alkylthiazole)s, and NiO/poly(4-alkylthiazole)s. (b) Schematic illustration of the formation process of the heterojunction interface and the hole transfer pathway from polymer to NiO.

heterojunction interface based on the Fermi level (E_F) alignment between NiO and poly(4-alkylthiazole)s.[54,55] A type II heterojunction is formed as a result of the staggered gradient energy levels.[56,57]

Figure 4b depicts the formation process and the internal hole transfer pathway of the composite photocathodes. Operated in this configuration, the photoexcited electron and hole can be spatially separated because the NiO layer provides a driving force for hole transport from poly(4-alkylthiazole)s to NiO,[58] resulting in the ameliorated photocurrent observed at the heterojunctions. Modification with HER co-catalysts may be a strategy to further improve the performance of hybrid electrodes if sufficient charge carrier extraction is ensured to significantly exceed the dark current contribution from the co-catalyst (Figure S9 of the Supporting Information).

CONCLUSION

With reference to the band edge alignment assumption, we have constructed hybrid inorganic–polymer photocathodes by coupling NiO nanosheets with a poly(4-alkylthiazole) layer. The poly(4-alkylthiazole)s serve directly as the heterojunction partner here. Combining poly(4-alkylthiazole)s to p-NiO manifested in a significantly raised PEC performance; i.e., the hybrid photocathodes display higher stability and an approximately 400 mV anodic shift of the onset potential. The net photocurrent of the NiO/PTzTNB and NiO/PTzTHX photocathodes presents extraordinary 4.6- and 5.7-fold enhancement in comparison to pristine NiO, which is also being equivalent to a 5.3- and 2-fold enhancement if compared

https://dx.doi.org/10.1021/acsami.0c03975
ACS Appl. Mater. Interfaces 2020, 12, 29173−29180

to bare PTzTNB and PTzTHX, respectively. Kinetic analysis demonstrates the synergy between NiO and poly(4-alkylthiazole)s stemming from the interface interaction. The type II alignment alleviates the recombination loss and enhances the carrier separation. We emphasize the interfacial interaction on the mitigation of charge carrier recombination for inorganic/organic polymer-based hybrid photocathodes.

■ ASSOCIATED CONTENT

Supporting Information

The Supporting Information is available free of charge at https://pubs.acs.org/doi/10.1021/acsami.0c03975.

PXRD patterns and SEM image of the NiO photocathode and digital photo of the NiO photocathode (Figure S1), LSV and CA curves of pristine PTzTNB and PTzTHX photocathodes (Figure S2), comparison of LSV curves of FTO and the photocathodes (Figure S3), continuous AM 1.5G illumination CA measurement of pristine PTzTHB (Figure S4), LSV curves of NiO/PTzTNB and NiO/PTzTHX photocathodes (Figure S5), EIS Nyquist plots of PTzTNB and PTzTHX photocathodes (Figure S6), net photocurrent density of NiO and NiO/PTzTNB photocathodes documented in the electrolyte with and without an electron scavenger (Figure S7), charge separation efficiency and charge transfer efficiency of NiO and NiO/PTzTNB photocathodes (Figure S8), and LSV curves for Pt-modified electrodes (Figure S9) (PDF)

■ AUTHOR INFORMATION

Corresponding Author

Adam Slabon − *Department of Materials and Environmental Chemistry, Stockholm University, 10691 Stockholm, Sweden;* orcid.org/0000-0002-4452-1831; Email: adam.slabon@mmk.su.se

Authors

Can Lu − *Institute of Inorganic Chemistry, RWTH Aachen University, D-52056 Aachen, Germany*

Zili Ma − *Institute of Inorganic Chemistry, RWTH Aachen University, D-52056 Aachen, Germany;* orcid.org/0000-0001-7975-9201

Jakob Jäger − *Institute of Organic Chemistry II and Advanced Materials, University of Ulm, D-89081 Ulm, Germany; Carl Zeiss Jena GmbH, Zeiss Group, D-73447 Oberkochen, Germany*

Tetyana M. Budnyak − *Department of Materials and Environmental Chemistry, Stockholm University, 10691 Stockholm, Sweden;* orcid.org/0000-0003-2112-9308

Richard Dronskowski − *Institute of Inorganic Chemistry, RWTH Aachen University, D-52056 Aachen, Germany; Hoffmann Institute of Advanced Materials, Shenzhen Polytechnic, Shenzhen, Guangdong 518055, People's Republic of China;* orcid.org/0000-0002-1925-9624

Anna Rokicińska − *Faculty of Chemistry, Jagiellonian University, 30-387 Krakow, Poland*

Piotr Kuśtrowski − *Faculty of Chemistry, Jagiellonian University, 30-387 Krakow, Poland*

Frank Pammer − *Institute of Organic Chemistry II and Advanced Materials, University of Ulm, D-89081 Ulm, Germany;* orcid.org/0000-0002-3869-0196

Complete contact information is available at: https://pubs.acs.org/10.1021/acsami.0c03975

Notes

The authors declare no competing financial interest.

■ ACKNOWLEDGMENTS

Can Lu appreciates the China Scholarship Council (CSC) for a Ph.D. scholarship. The authors thank Professor Ulrich Simon for access to electron microscopy facilities. Adam Slabon thanks Vinnova, the Swedish innovation agency, for financial support (Project C1Bio 2019-03174). The XPS measurements were carried out with the equipment purchased with the financial support of the European Regional Development Fund in the framework of the Polish Innovation Operational Program (Contract POIG.02.01.00-12-023/08).

■ REFERENCES

(1) Zhang, H.; An, P.; Zhou, W.; Guan, B. Y.; Zhang, P.; Dong, J.; Lou, X. W. D. Dynamic Traction of Lattice-Confined Platinum Atoms into Mesoporous Carbon Matrix for Hydrogen Evolution Reaction. *Sci. Adv.* **2018**, *4*, eaao6657.

(2) Hisatomi, T.; Domen, K. Reaction Systems for Solar Hydrogen Production via Water Splitting with Particulate Semiconductor Photocatalysts. *Nat. Catal.* **2019**, *2*, 387−399.

(3) Kirner, J. T.; Finke, R. G. Water-Oxidation Photoanodes Using Organic Light-Harvesting Materials: A Review. *J. Mater. Chem. A* **2017**, *5*, 19560−19592.

(4) Lee, D. K.; Lee, D.; Lumley, M. A.; Choi, K.-S. Progress on Ternary Oxide-Based Photoanodes for Use in Photoelectrochemical Cells for Solar Water Splitting. *Chem. Soc. Rev.* **2019**, *48*, 2126−2157.

(5) Ma, Z.; Jaworski, A.; George, J.; Rokicinska, A.; Thersleff, T.; Budnyak, T. M.; Hautier, G.; Pell, A. J.; Dronskowski, R.; Kuśtrowski, P.; Slabon, A. Exploring the Origins of Improved Photocurrent by Acidic Treatment for Quaternary Tantalum-Based Oxynitride Photoanodes on the Example of $CaTaO_2N$. *J. Phys. Chem. C* **2020**, *124*, 152−160.

(6) Hu, C.; Zhang, L.; Gong, J. Recent Progress Made in the Mechanism Comprehension and Design of Electrocatalysts for Alkaline Water Splitting. *Energy Environ. Sci.* **2019**, *12*, 2620−2645.

(7) Davi, M.; Mann, M.; Ma, Z.; Schrader, F.; Drichel, A.; Budnyk, S.; Rokicinska, A.; Kustrowski, P.; Dronskowski, R.; Slabon, A. An MnNCN-Derived Electrocatalyst for $CuWO_4$ Photoanodes. *Langmuir* **2018**, *34*, 3845−3852.

(8) Vanka, S.; Arca, E.; Cheng, S.; Sun, K.; Botton, G. A.; Teeter, G.; Mi, Z. High Efficiency Si Photocathode Protected by Multifunctional GaN Nanostructures. *Nano Lett.* **2018**, *18*, 6530−6537.

(9) Ma, Z.; Linnenberg, O.; Rokicinska, A.; Kustrowski, P.; Slabon, A. Augmenting the Photocurrent of $CuWO_4$ Photoanodes by Heat Treatment in the Nitrogen Atmosphere. *J. Phys. Chem. C* **2018**, *122*, 19281−19288.

(10) Hill, J. C.; Landers, A. T.; Switzer, J. A. An Electrodeposited Inhomogeneous Metal−Insulator−Semiconductor Junction for Efficient Photoelectrochemical Water Oxidation. *Nat. Mater.* **2015**, *14*, 1150−1155.

(11) Ma, Z.; Thersleff, T.; Görne, A. L.; Cordes, N.; Liu, Y.; Jakobi, S.; Rokicinska, A.; Schichtl, Z. G.; Coridan, R. H.; Kustrowski, P.; Schnick, W.; Dronskowski, R.; Slabon, A. Quaternary Core−Shell Oxynitride Nanowire Photoanode Containing a Hole-Extraction Gradient for Photoelectrochemical Water Oxidation. *ACS Appl. Mater. Interfaces* **2019**, *11*, 19077−19086.

(12) Lu, C.; Jothi, P. R.; Thersleff, T.; Budnyak, T. M.; Rokicinska, A.; Yubuta, K.; Dronskowski, R.; Kuśtrowski, P.; Fokwa, B. P. T.; Slabon, A. Nanostructured Core−Shell Metal Borides−Oxides as Highly Efficient Electrocatalysts for Photoelectrochemical Water Oxidation. *Nanoscale* **2020**, *12*, 3121−3128.

(13) Jin, L.; Alotaibi, B.; Benetti, D.; Li, S.; Zhao, H. G.; Mi, Z.; Vomiero, A.; Rosei, F. Near-Infrared Colloidal Quantum Dots for

Efficient and Durable Photoelectrochemical Solar-Driven Hydrogen Production. *Adv. Sci.* **2016**, *3*, 1500345.
(14) Roger, I.; Shipman, M. A.; Symes, M. D. Earth-Abundant Catalysts for Electrochemical and Photoelectrochemical Water Splitting. *Nat. Rev. Chem.* **2017**, *1*, 0003.
(15) Yang, W.; Prabhakar, R. R.; Tan, J.; Tilley, S. D.; Moon, J. Strategies for Enhancing the Photocurrent, Photovoltage, and Stability of Photoelectrodes for Photoelectrochemical Water Splitting. *Chem. Soc. Rev.* **2019**, *48*, 4979−5015.
(16) Kim, J. H.; Hansora, D.; Sharma, P.; Jang, J. W.; Lee, J. S. Toward Practical Solar Hydrogen Production-an Artificial Photosynthetic Leaf-to-Farm Challenge. *Chem. Soc. Rev.* **2019**, *48*, 1908−1971.
(17) Sim, U.; Moon, J.; An, J.; Kang, J. H.; Jerng, S. E.; Moon, J.; Cho, S. P.; Hong, B. H.; Nam, K. T. N-Doped Graphene Quantum Sheets on Silicon Nanowire Photocathodes for Hydrogen Production. *Energy Environ. Sci.* **2015**, *8*, 1329−1338.
(18) Ertl, M.; Ma, Z.; Thersleff, T.; Lyu, P.; Huettner, S.; Nachtigall, P.; Breu, J.; Slabon, A. Mössbauerite as Iron-Only Layered Oxyhydroxide Catalyst for WO_3 Photoanodes. *Inorg. Chem.* **2019**, *58*, 9655−9662.
(19) Shi, Y.; Gimbert-Suriñach, C.; Han, T.; Berardi, S.; Lanza, M.; Llobet, A. CuO-Functionalized Silicon Photoanodes for Photoelectrochemical Water Splitting Devices. *ACS Appl. Mater. Interfaces* **2016**, *8*, 696−702.
(20) Chen, C. J.; Liu, C. W.; Yang, K. C.; Yin, L. C.; Wei, D. H.; Hu, S. F.; Liu, R. S. Amorphous Phosphorus-Doped Cobalt Sulfide Modified on Silicon Pyramids for Efficient Solar Water Reduction. *ACS Appl. Mater. Interfaces* **2018**, *10*, 37142−37149.
(21) Kim, B.; Park, G. S.; Hwang, Y. J.; Won, D. H.; Kim, W.; Lee, D. K.; Min, B. K. $Cu(In,Ga)(S,Se)_2$ Photocathodes with a Grown-In Cu_xS Catalyst for Solar Water Splitting. *ACS Energy Lett.* **2019**, *4*, 2937−2944.
(22) Sun, X.; Jiang, J.; Yang, Y.; Shan, Y.; Gong, L.; Wang, M. Enhancing the Performance of Si-Based Photocathodes for Solar Hydrogen Production in Alkaline Solution by Facilely Intercalating a Sandwich N-Doped Carbon Nanolayer to the Interface of Si and TiO_2. *ACS Appl. Mater. Interfaces* **2019**, *11*, 19132−19140.
(23) Pan, Q.; Chen, T.; Ma, L.; Wang, G.; Hu, W.-B.; Zou, Z.; Wen, K.; Yang, H. Covalent Triazine-Based Polymers with Controllable Band Alignment Matched with $BiVO_4$ To Boost Photogeneration of Holes for Water Splitting. *Chem. Mater.* **2019**, *31*, 8062−8068.
(24) Liras, M.; Barawi, M.; De La Peña O'Shea, V. A. Hybrid Materials Based on Conjugated Polymers and Inorganic Semiconductors as Photocatalysts: From Environmental to Energy Applications. *Chem. Soc. Rev.* **2019**, *48*, 5454−5487.
(25) Srinivasan, N.; Shiga, Y.; Atarashi, D.; Sakai, E.; Miyauchi, M. A PEDOT-Coated Quantum Dot as Efficient Visible Light Harvester for Photocatalytic Hydrogen Production. *Appl. Catal., B* **2015**, *179*, 113−121.
(26) Xu, N.; Li, F.; Gao, L.; Hu, H.; Hu, Y.; Long, X.; Ma, J.; Jin, J. Polythiophene Coated $CuBi_2O_4$ Networks: A Porous Inorganic−Organic Hybrid Heterostructure for Enhanced Photoelectrochemical Hydrogen Evolution. *Int. J. Hydrogen Energy* **2018**, *43*, 2064−2072.
(27) Jäger, J.; Tchamba Yimga, N.; Urdanpilleta, M.; von Hauff, E.; Pammer, F. Toward N-Type Analogues to Poly(3-Alkylthiophene)s: Influence of Side-Chain Variation on Bulk-Morphology and Electron Transport Characteristics of Head-to-Tail Regioregular Poly(4-Alkylthiazole)S. *J. Mater. Chem. C* **2016**, *4*, 2587−2597.
(28) Pammer, F.; Jäger, J.; Rudolf, B.; Sun, Y. Soluble Head-to-Tail Regioregular Polythiazoles: Preparation, Properties, and Evidence for Chain-Growth Behavior in the Synthesis via Kumada-Coupling Polycondensation. *Macromolecules* **2014**, *47*, 5904−5912.
(29) Jiang, C.; Reyes-Lillo, S. E.; Liang, Y.; Liu, Y.-S.; Liu, G.; Toma, F. M.; Prendergast, D.; Sharp, I. D.; Cooper, J. K. Electronic Structure and Performance Bottlenecks of $CuFeO_2$ Photocathodes. *Chem. Mater.* **2019**, *31*, 2524−2534.
(30) Wen, P.; Sun, Y.; Li, H.; Liang, Z.; Wu, H.; Zhang, J.; Zeng, H.; Geyer, S. M.; Jiang, L. A Highly Active Three-Dimensional Z-Scheme $ZnO/Au/g\text{-}C_3N_4$ Photocathode for Efficient Photoelectrochemical Water Splitting. *Appl. Catal., B* **2020**, *263*, 118180.
(31) Luo, X. F.; Hu, X.; Zhao, X. Y.; Goh, S. H.; Li, X. D. Miscibility and Interactions in Blends and Complexes of Poly(4-Methyl-5-Vinylthiazole) with Proton-Donating Polymers. *Polymer* **2003**, *44*, 5285−5291.
(32) Hu, H.; Qiao, M.; Xie, F.; Fan, K.; Lei, H.; Tan, D.; Bao, X.; Lin, H.; Zong, B.; Zhang, X. Comparative X-Ray Photoelectron Spectroscopic Study on the Desulfurization of Thiophene by Raney Nickel and Rapidly Quenched Skeletal Nickel. *J. Phys. Chem. B* **2005**, *109*, 5186−5192.
(33) Martinez, A. M.; Arriaga, L. G.; Fernández, A. M.; Cano, U. Band Edges Determination of $CuInS_2$ Thin Films Prepared by Electrodeposition. *Mater. Chem. Phys.* **2004**, *88*, 417−420.
(34) Cardona, C. M.; Li, W.; Kaifer, A. E.; Stockdale, D.; Bazan, G. C. Electrochemical Considerations for Determining Absolute Frontier Orbital Energy Levels of Conjugated Polymers for Solar Cell Applications. *Adv. Mater.* **2011**, *23*, 2367−2371.
(35) Wang, Q.-K.; Wang, R.-B.; Shen, P.-F.; Li, C.; Li, Y.-Q.; Liu, L.-J.; Duhm, S.; Tang, J.-X. Energy Level Offsets at Lead Halide Perovskite/Organic Hybrid Interfaces and Their Impacts on Charge Separation. *Adv. Mater. Interfaces* **2015**, *2*, 1400528.
(36) Wick-Joliat, R.; Musso, T.; Prabhakar, R. R.; Löckinger, J.; Siol, S.; Cui, W.; Sévery, L.; Moehl, T.; Suh, J.; Hutter, J.; Iannuzzi, M.; Tilley, S. D. Stable and Tunable Phosphonic Acid Dipole Layer for Band Edge Engineering of Photoelectrochemical and Photovoltaic Heterojunction Devices. *Energy Environ. Sci.* **2019**, *12*, 1901−1909.
(37) Wang, Q.; Wang, X.; Yu, Z.; Jiang, X.; Chen, J.; Tao, L.; Wang, M.; Shen, Y. Artificial Photosynthesis of Ethanol Using Type-II $g\text{-}C_3N_4/ZnTe$ Heterojunction in Photoelectrochemical CO_2 Reduction System. *Nano Energy* **2019**, *60*, 827−835.
(38) Zhong, M.; Hisatomi, T.; Kuang, Y.; Zhao, J.; Liu, M.; Iwase, A.; Jia, Q.; Nishiyama, H.; Minegishi, T.; Nakabayashi, M.; Shibata, N.; Niishiro, R.; Katayama, C.; Shibano, H.; Katayama, M.; Kudo, A.; Yamada, T.; Domen, K. Surface Modification of CoO_x Loaded $BiVO_4$ Photoanodes with Ultrathin p-Type NiO Layers for Improved Solar Water Oxidation. *J. Am. Chem. Soc.* **2015**, *137*, 5053−5060.
(39) Chen, J.; Tao, X.; Tao, L.; Li, H.; Li, C.; Wang, X.; Li, C.; Li, R.; Yang, Q. Novel Conjugated Organic Polymers as Candidates for Visible-Light-Driven Photocatalytic Hydrogen Production. *Appl. Catal., B* **2019**, *241*, 461−470.
(40) Nail, B. A.; Fields, J. M.; Zhao, J.; Wang, J.; Greaney, M. J.; Brutchey, R. L.; Osterloh, F. E. Nickel Oxide Particles Catalyze Photochemical Hydrogen Evolution from Water-Nanoscaling Promotes p-Type Character and Minority Carrier Extraction. *ACS Nano* **2015**, *9*, 5135−5142.
(41) Su, X.; Chen, Y.; Ren, L.; He, Y.; Yin, X.; Liu, Y.; Yang, W. Cobalt Catalyst Grafted CdSeTe Quantum Dots on Porous NiO as Photocathode for H_2 Evolution under Visible Light. *ACS Sustainable Chem. Eng.* **2019**, *7*, 11166−11174.
(42) Li, C.; Li, Y.; Delaunay, J. J. A Novel Method to Synthesize Highly Photoactive Cu_2O Microcrystalline Films for Use in Photoelectrochemical Cells. *ACS Appl. Mater. Interfaces* **2014**, *6*, 480−486.
(43) Lai, L.-H.; Gomulya, W.; Berghuis, M.; Protesescu, L.; Detz, R. J.; Reek, J. N. H.; Kovalenko, M. V.; Loi, M. A. Organic−Inorganic Hybrid Solution-Processed H_2-Evolving Photocathodes. *ACS Appl. Mater. Interfaces* **2015**, *7*, 19083−19090.
(44) Yao, L.; Guijarro, N.; Boudoire, F.; Liu, Y.; Rahmanudin, A.; Wells, R. A.; Sekar, A.; Cho, H.-H.; Yum, J.-H.; Le Formal, F.; Sivula, K. Establishing Stability in Organic Semiconductor Photocathodes for Solar Hydrogen Production. *J. Am. Chem. Soc.* **2020**, *142*, 7795−7802.
(45) Luo, J.; Steier, L.; Son, M.; Schreier, M.; Mayer, M. T.; Grätzel, M. Cu_2O Nanowire Photocathodes for Efficient and Durable Solar Water Splitting. *Nano Lett.* **2016**, *16*, 1848−1857.
(46) Ma, M.; Zhang, K.; Li, P.; Jung, M. S.; Jeong, M. J.; Park, J. H. Dual Oxygen and Tungsten Vacancies on a WO_3 Photoanode for Enhanced Water Oxidation. *Angew. Chem., Int. Ed.* **2016**, *55*, 11819−11823.

https://dx.doi.org/10.1021/acsami.0c03975
ACS Appl. Mater. Interfaces 2020, 12, 29173−29180

(47) Yang, Y.; Wang, M.; Zhang, P.; Wang, W.; Han, H.; Sun, L. Evident Enhancement of Photoelectrochemical Hydrogen Production by Electroless Deposition of M-B (M = Ni, Co) Catalysts on Silicon Nanowire Arrays. *ACS Appl. Mater. Interfaces* **2016**, *8*, 30143−30151.
(48) Corby, S.; Pastor, E.; Dong, Y.; Zheng, X.; Francàs, L.; Sachs, M.; Selim, S.; Kafizas, A.; Bakulin, A. A.; Durrant, J. R. Charge Separation, Band-Bending, and Recombination in WO_3 Photoanodes. *J. Phys. Chem. Lett.* **2019**, *10*, 5395−5401.
(49) Ye, K.-H.; Li, H.; Huang, D.; Xiao, S.; Qiu, W.; Li, M.; Hu, Y.; Mai, W.; Ji, H.; Yang, S. Enhancing Photoelectrochemical Water Splitting by Combining Work Function Tuning and Heterojunction Engineering. *Nat. Commun.* **2019**, *10*, 3687.
(50) Ma, L.; Fan, H.; Wang, J.; Zhao, Y.; Tian, H.; Dong, G. Water-Assisted Ions in Situ Intercalation for Porous Polymeric Graphitic Carbon Nitride Nanosheets with Superior Photocatalytic Hydrogen Evolution Performance. *Appl. Catal., B* **2016**, *190*, 93−102.
(51) Cui, J.; Qi, Y.; Dong, B.; Mu, L.; Ding, Q.; Liu, G.; Jia, M.; Zhang, F.; Li, C. One-Pot Synthesis of $BaMg_{1/3}Ta_{2/3}O_{3-x}N_y/Ta_3N_5$ Heterostructures as H_2-Evolving Photocatalysts for Construction of Visible-Light-Driven Z-Scheme Overall Water Splitting. *Appl. Catal., B* **2019**, *241*, 1−7.
(52) Wang, N.; Liu, M.; Tan, H.; Liang, J.; Zhang, Q.; Wei, C.; Zhao, Y.; Sargent, E. H.; Zhang, X. Compound Homojunction:Heterojunction Reduces Bulk and Interface Recombination in ZnO Photoanodes for Water Splitting. *Small* **2017**, *13*, 1603527.
(53) Liu, G.; Ye, S.; Yan, P.; Xiong, F.; Fu, P.; Wang, Z.; Chen, Z.; Shi, J.; Li, C. Enabling an Integrated Tantalum Nitride Photoanode to Approach the Theoretical Photocurrent Limit for Solar Water Splitting. *Energy Environ. Sci.* **2016**, *9*, 1327−1334.
(54) He, C.; Zhang, J. H.; Zhang, W. X.; Li, T. T. Type-II InSe/g-C_3N_4 Heterostructure as a High-Efficiency Oxygen Evolution Reaction Catalyst for Photoelectrochemical Water Splitting. *J. Phys. Chem. Lett.* **2019**, *10*, 3122−3128.
(55) Lin, J.; Yu, Y.; Zhang, Z.; Gao, F.; Liu, S.; Wang, W.; Li, G. A Novel Approach for Achieving High-Efficiency Photoelectrochemical Water Oxidation in InGaN Nanorods Grown on Si System: MXene Nanosheets as Multifunctional Interfacial Modifier. *Adv. Funct. Mater.* **2020**, *30*, 1910479.
(56) Liu, H.; Tan, Y.; Cao, M.; Hu, H.; Wu, L.; Yu, X.; Wang, L.; Sun, B.; Zhang, Q. Fabricating $CsPbX_3$-Based Type I and Type II Heterostructures by Tuning the Halide Composition of Janus $CsPbX_3/ZrO_2$ Nanocrystals. *ACS Nano* **2019**, *13*, 5366−5374.
(57) Monny, S. A.; Zhang, L.; Wang, Z.; Luo, B.; Konarova, M.; Du, A.; Wang, L. Fabricating Highly Efficient Heterostructured $CuBi_2O_4$ Photocathodes for Unbiased Water Splitting. *J. Mater. Chem. A* **2020**, *8*, 2498−2504.
(58) Shan, B.; Sherman, B. D.; Klug, C. M.; Nayak, A.; Marquard, S. L.; Liu, Q.; Bullock, R. M.; Meyer, T. J. Modulating Hole Transport in Multilayered Photocathodes with Derivatized p-Type Nickel Oxide and Molecular Assemblies for Solar-Driven Water Splitting. *J. Phys. Chem. Lett.* **2017**, *8*, 4374−4379.

https://dx.doi.org/10.1021/acsami.0c03975
ACS Appl. Mater. Interfaces 2020, 12, 29173−29180